

University of Groningen

Robust Inhibition-Augmented Operator for Delineation of Curvilinear Structures

Strisciuglio, Nicola; Azzopardi, George; Petkov, Nicolai

Published in:
ieee transactions on image processing

DOI:
[10.1109/TIP.2019.2922096](https://doi.org/10.1109/TIP.2019.2922096)

IMPORTANT NOTE: You are advised to consult the publisher's version (publisher's PDF) if you wish to cite from it. Please check the document version below.

Document Version
Publisher's PDF, also known as Version of record

Publication date:
2019

[Link to publication in University of Groningen/UMCG research database](#)

Citation for published version (APA):

Strisciuglio, N., Azzopardi, G., & Petkov, N. (2019). Robust Inhibition-Augmented Operator for Delineation of Curvilinear Structures. *ieee transactions on image processing*, 28(12), 5852-5866.
<https://doi.org/10.1109/TIP.2019.2922096>

Copyright

Other than for strictly personal use, it is not permitted to download or to forward/distribute the text or part of it without the consent of the author(s) and/or copyright holder(s), unless the work is under an open content license (like Creative Commons).

The publication may also be distributed here under the terms of Article 25fa of the Dutch Copyright Act, indicated by the "Taverne" license. More information can be found on the University of Groningen website: <https://www.rug.nl/library/open-access/self-archiving-pure/taverne-amendment>.

Take-down policy

If you believe that this document breaches copyright please contact us providing details, and we will remove access to the work immediately and investigate your claim.

Downloaded from the University of Groningen/UMCG research database (Pure): <http://www.rug.nl/research/portal>. For technical reasons the number of authors shown on this cover page is limited to 10 maximum.

Robust Inhibition-Augmented Operator for Delineation of Curvilinear Structures

Nicola Strisciuglio^{ID}, George Azzopardi^{ID}, and Nicolai Petkov^{ID}

Abstract—Delineation of curvilinear structures in images is an important basic step of several image processing applications, such as segmentation of roads or rivers in aerial images, vessels or staining membranes in medical images, and cracks in pavements and roads, among others. Existing methods suffer from insufficient robustness to noise. In this paper, we propose a novel operator for the detection of curvilinear structures in images, which we demonstrate to be robust to various types of noise and effective in several applications. We call it RUSTICO, which stands for RobUST Inhibition-augmented Curvilinear Operator. It is inspired by the push-pull inhibition in visual cortex and takes as input the responses of two trainable B-COSFIRE filters of opposite polarity. The output of RUSTICO consists of a magnitude map and an orientation map. We carried out experiments on a data set of synthetic stimuli with noise drawn from different distributions, as well as on several benchmark data sets of retinal fundus images, crack pavements, and aerial images and a new data set of rose bushes used for automatic gardening. We evaluated the performance of RUSTICO by a metric that considers the structural properties of line networks (connectivity, area, and length) and demonstrated that RUSTICO outperforms many existing methods with high statistical significance. RUSTICO exhibits high robustness to noise and texture.

Index Terms—Curvilinear structures, delineation, non-linear filtering, noise inhibition, orientation map.

I. INTRODUCTION

THE automatic detection of curvilinear and elongated patterns in images is an important step in many image processing applications: segmentation of rivers and roads in aerial images [1] (Fig. 1a), cracks in walls and roads [2] (Fig. 1b), palm-print lines for biometric applications (Fig. 1c), staining cell membranes [3], and blood vessels in computer-tomography [4] images (Fig. 1e and Fig. 1f, respectively), among others. A novel application in the field of gardening robotics requires the localization and segmentation of rose stems and branches with the purpose of automated cutting by using a vision-servoed robotic arm. The detection of branches in rose buds is challenging due to the highly textured appearance of gardens (Fig. 1d). In all mentioned applications, one of the main problems is the design of robust algorithms for the detection and segmentation of elongated patterns

Manuscript received October 25, 2018; revised April 29, 2019; accepted May 27, 2019. Date of publication June 21, 2019; date of current version August 30, 2019. This work was supported by the EU H2020 Research and Innovation Program under Grant 688007 (TrimBot2020). The associate editor coordinating the review of this manuscript and approving it for publication was Prof. Tolga Tasdizen. (*Corresponding author: Nicola Strisciuglio.*)

The authors are with the Bernoulli Institute for Mathematics, Computer Science and Artificial Intelligence, University of Groningen, 9747 AG Groningen, The Netherlands (e-mail: n.strisciuglio@rug.nl).

Digital Object Identifier 10.1109/TIP.2019.2922096

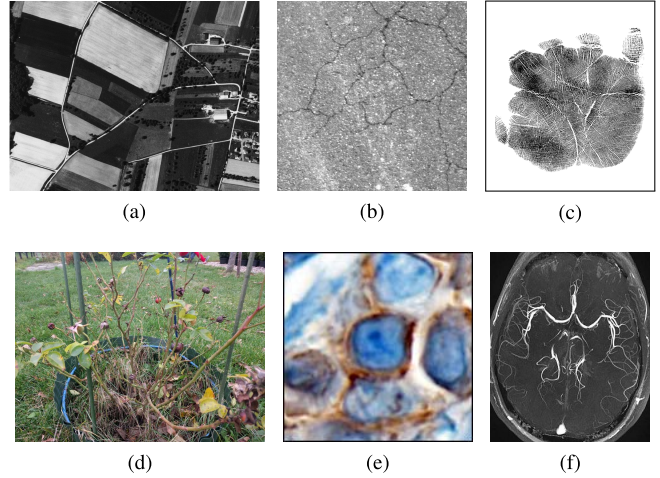


Fig. 1. Example images where delineation of curvilinear structures is important: (a) an aerial image of a countryside area for extraction of road networks, (b) a road surface image for detection of cracks, (c) a palm-print scan for biometric applications, (d) a rose bush for detection of branches, (e) a microscopy image for the segmentation of staining-cell membrane, and (f) a CT scan of the brain for the delineation of blood vessels.

(i.e. lines and bars) with certain appearance properties, such as color, thickness and tortuosity surrounded by a highly noisy background. In this work, we use the term ‘noise’ to indicate spurious signals introduced by textures present in the background around the patterns of interest.

State-of-the-art approaches for the delineation of curvilinear patterns in images were recently surveyed in [5]. Existing methods are based on different techniques ranging from parametric to point processes and machine learning approaches, as well as region growing, filtering and mathematical morphology. We review these methods in the following of the section. The Hough transform is a well-known parametric method, which projects an input image into a parameter space where line segments can be better detected. It is based on mathematical modeling of the patterns of interest (for lines two parameters are used, namely the slope and the bias of a straight line). In order to detect other types of pattern, such as circles or lines of certain curvatures, different mathematical models have to be provided to the transform operator. This approach requires a-priori knowledge about the shape of the patterns of interest and it is not suitable to detect curvilinear structures of arbitrary shapes.

Methods that employ point processes were proposed to segment line networks, with a particular focus to aerial images, by tracking elongated patterns with the use of complex

mathematical models. In [6], line networks are considered as a set of interacting line segments and reconstructed with point processes. Combinations of point processes with Monte-Carlo simulation and Gibbs models were proposed in [7] and [8], respectively. The accuracy of segmentation was further improved by combining point processes with graph-based representations in [9] and [10]. A method that employs a graph-based representation, which takes into account the topology of the line-networks was proposed in [11]. These methods have high computational complexity and are not suitable for real-time applications or for processing of high resolution images.

Machine learning techniques have also been used to construct methods for classification of image pixels as belonging or not belonging to curvilinear structures. Multi-scale Gaussian and Gabor wavelet features were used to form pixel-wise feature vectors in combination with a k -NN and a Bayesian classifiers in [12] and [13], respectively. In [14], a feature vector was formed with the responses of a bank of ridge detectors. A line operator was introduced in [15] and used to extract features and form vectors that are fed to a Support Vector Machine (SVM) classifier. In [16], the authors computed moment-invariant features and applied a multilayer neural network to perform pixel-wise classification of input images. More recent approaches employ deep convolutional neural networks (CNNs) to learn effective features directly from training data. Various architectures from segmentation of images have been proposed, with application to medical data, namely U-net [17], or urban environments, namely SegNet [18]. Edge detection has also received the interest of the CNN research community and various architectures were proposed, such as Holistically-nested Edge Detection (HED) [19], DeepContour [20] and Deep Crisp Boundaries [21]. Although achieving high accuracies, these methods require intensive training procedures on large amount of labeled data to learn effective models of the patterns of interest. In that respect, obtaining pixel-wise labeling of images of line networks is usually a time consuming and expensive process. Moreover, the resulting classification models may not be easily transferable to other applications where training data is not readily available.

Approaches based on filtering or mathematical morphology techniques were proposed as more practical and simple solutions for the delineation of curvilinear patterns in images. Some of these methods use local derivatives in multi-scale analysis also in 3D images [22]–[24] or model the profile of elongated patterns by means of two-dimensional Gaussian kernels, called matched filters [25], [26]. Other methods use mathematical morphology and *a-priori* knowledge about the structure of the line networks [27], [28]. A region growing procedure that combines information about the size, width and orientation of lines was introduced in [29], while a method based on line-concavity analysis was proposed in [30]. In [31], the authors combine an infinite active contour model with intensity information and local phase based enhancement map to improve segmentation performance while preserving vessel edges. In previous works [32]–[34], we introduced trainable filters selective for lines and line-endings and showed that

effective delineation of elongated patterns can be obtained by combining their responses. Recently, a method for curvilinear structure analysis based on ranking the orientation responses of morphological path operators, called RORPO, was proposed for 2D [35] and 3D images [36]. Filters based on orientation scores, which are 3-dimensional functions in the domains of position and orientation, were proposed in [37].

In this paper, we propose a novel operator for the delineation of curvilinear structures in images. We named it RUSTICO, which stands for RobUST Inhibition-augmented Curvilinear Operator. Its design is based on top of the *B*-COSFIRE filters [32], which we augmented with a neuro-physiological mechanism of push-pull inhibition, exhibited by some neurons in the visual system (see Section II). RUSTICO is a filtering-based approach for delineation of curvilinear structure, but differs from methods of the same category on several aspects. It is embedded with a brain-inspired push-pull inhibition component that improves the robustness of the detection of curvilinear patterns to various types of noise and spurious texture. The inhibition component is independent of the specific type of noise present in the image, thus not requiring an external denoising technique that makes a hypothesis on the model of the noise. Furthermore, RUSTICO is trainable. Its selectivity for patterns of interest is, indeed, not pre-fixed in the implementation as happens in other existing approaches, but it is automatically determined by a configuration process performed on a prototype example. This aspect provides flexibility and applicability of the proposed filtering framework for the detection of different patterns of interest without the need of creating mathematical models or designing specific filter kernels or structuring elements.

We demonstrate the effectiveness of the proposed method on benchmark data sets of images taken with different modalities and for different applications: detection of roads and rivers in aerial images, delineation of cracks in roads, segmentation of rose stems in gardens and segmentation of vessels in retinal images. It is worth pointing out that obtaining ground truth images for the delineation of curvilinear patterns in real images is a time-consuming and expensive process, thus limiting the size of real image data sets. Furthermore, we study the robustness of RUSTICO with respect to different kinds and levels of image noise and to patterns with high curvature points by experimenting on synthetic data that we created.

II. RATIONALE AND CONTRIBUTIONS

For the design of RUSTICO, we took inspiration from the *push-pull* inhibition phenomenon that is exhibited by some neurons in area V1 of the visual cortex. Such a neuron is excited by a stimulus of preferred orientation and contrast, while a stimulus with the same orientation and opposite contrast suppresses its response. There is neurophysiological evidence that neurons that present this kind of inhibition have better selectivity to elongated structures [38]. In this work, we combine the results of neurophysiology research with image processing techniques to design a novel operator, called RUSTICO, that is robust to noisy and textured stimuli.

The fundamental idea behind the formulation of RUSTICO is to employ an inhibition mechanism to suppress the

responses caused by image noise and texture. RUSTICO consists of two main components, namely an **excitatory part**, based on the framework of the *B-COSFIRE* filter, and a **novel inhibitory component**. The excitatory component is selective for bright lines on dark background, while the inhibitory counterpart is selective for wider dark lines on bright background. They are composed of the same number of sub-units (i.e. basic filters): each excitatory unit has an inhibitory counterpart, usually of larger size, whose areas of support overlap each other. The push-pull inhibition phenomenon is **extensively described in the neuro-physiology research literature** [39], [40].

The type of inhibition included in RUSTICO, referred to as push-pull, is known to occur in certain neurons of area V1 and differs from other inhibition mechanisms exhibited by neurons in subsequent areas of the visual system. As we demonstrate in Section IV, this configuration allows the suppression of noise along curvilinear structures. Another form of inhibition, which is exhibited by shape-selective neurons in area TEO [41], involves neurons whose receptive fields (in image processing terminology a filter represents a neuron and area of support represents the receptive field of the neuron) do not overlap each other. **That type of inhibition allows to discriminate between patterns that are parts of others; e.g. the letter F is part of the letter E.** A computational model for this phenomenon was implemented in [42], [43]. The two types of inhibition serve different purposes: push-pull inhibition that we implement in RUSTICO serves to **suppress noise**, while the other serves to **distinguish better between patterns of interest**.

The response of RUSTICO is computed by first multiplying the inhibitory response with a weighting factor and then subtracting the result from the excitatory response. Its output consists of *a*) a magnitude map that provides localization and intensity of curvilinear patterns and *b*) an orientation map that gives an estimate of the orientation of curvilinear structures at each pixel.

The main contributions of this work are: *a*) a new RUSTICO algorithm for detection of curvilinear patterns that is robust to noise and texture, *b*) application examples in image processing pipelines for the analysis of images with different characteristics, *c*) an extended experimental study on various benchmark data sets of the performance of RUSTICO and the effect of push-pull inhibition for the delineation of curvilinear structures, *d*) and the release of a new labeled data set of garden images for testing rose stem detection algorithms.

III. METHOD

A. General Framework

The proposed operator is based on the framework of the existing *B-COSFIRE* filters. The response map of a *B-COSFIRE* filter is computed by combining the responses of a **Difference-of-Gaussians (DoG)** filter at certain positions with respect to its support center. The positions at which the DoG responses are taken are determined by an automatic configuration process performed on a **prototype pattern** of interest. Their **mutual spatial arrangement** determines the **selectivity** of the *B-COSFIRE* filter. Subsequently, the resulting *B-COSFIRE* filter can be applied in new images to detect

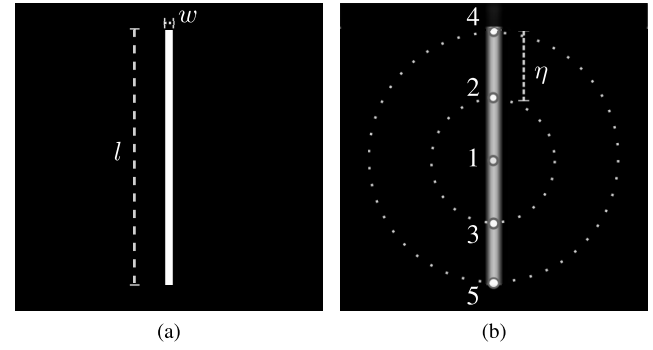


Fig. 2. Example of the configuration of a *B-COSFIRE* filter. (a) A line of length l and width w is used as a prototype pattern. (b) The position of local DoG maxima along concentric circles of increasing radii in steps of η pixels are considered to configure the *B-COSFIRE* model of the line in (a).

curvilinear structures. The *B-COSFIRE* filter approach is thus composed of two stages: configuration and application.

1) Configuration: Given a prototype pattern, such as a synthetic bar of width w and length l (Fig. 2a), we extract a representation of such pattern by an automatic configuration process. We first detect **changes of contrast** by using a *DoG* filter, which is formally defined as:

$$DoG_\sigma(x, y) = \frac{1}{2\pi(0.5\sigma)^2} e^{-\frac{x^2+y^2}{2(0.5\sigma)^2}} - \frac{1}{2\pi\sigma^2} e^{-\frac{x^2+y^2}{2\sigma^2}} \quad (1)$$

where the standard deviation of the outer Gaussian function is $\sigma = w/1.92$ [44], and (x, y) are the image coordinates. The DoG function has been accepted as a computational model of LGN cells in the visual system that respond to contrast changes [45], [46]. Motivated by neuro-physiological studies, we choose the standard deviation of the **inner Gaussian function of the DoG filter equal to 0.5σ** [47].

After choosing a reference point in the prototype pattern (point '1' in Fig. 2b), we consider a number of concentric circles (of increasing radii in steps of η pixels) around that point and **consider the positions of the local DoG maxima along those circles** (Fig. 2b). We represent each such position i with a 4-tuple $(\delta_i, \sigma_i, \rho_i, \phi_i)$, where $\delta_i \in \{-1, 1\}$ indicates the polarity of the DoG filter (-1 represents center-off and $+1$ represents center-on), σ_i is the standard deviation of its outer Gaussian function, ρ_i and ϕ_i are the polar coordinates of the considered point with respect to the reference point. We define the set of the selected DoG responses for a line prototype pattern of width w and preferred length l , like the one in Fig. 2a, as:

$$B = \{(\delta_i, \sigma_i = w/1.92, \rho_i, \phi_i)\}, i = 0, \dots, \lfloor l/\eta \rfloor + 1. \quad (2)$$

2) Application: In the application phase, the response $r_B(x, y)$ of a *B-COSFIRE* filter B is computed in five steps, namely *convolve-ReLU-blur-shift-combine*. In the first four steps we compute intermediate feature maps, which we fuse into one output map in the final step.

We first *convolve* an input image I with the DoG kernel DoG_{σ_i} , followed by a rectifier linear unit (*ReLU*) denoted

高斯
差分
濾波
兩個甚至更多
高斯核運算
結果圖的相減
往往能得
到角點、邊緣
等高圖

by $|\cdot|^+$, and define the resulting feature map $C_i(x, y)$ as:

$$C_i(x, y) = \left| \sum_{x' \in \Omega} \sum_{y' \in \Omega} I(x, y) DoG_{\sigma_i}(x - x', y - y') \right|^+ \quad (3)$$

where $\Omega = [-3\sigma_i, 3\sigma_i]$ indicates the size of the DoG kernel. Because we use only one DoG filter to configure a *B-COSFIRE* filter the σ_i in all tuples are the same. In practice we only apply one convolution of the input image with the concerned DoG filter and share the resulting response map among the subsequent operations required for each tuple.

Next, in order to account for some tolerance to deformations of the prototype pattern, we *blur* the DoG responses. The blur consists in a dilation of the image with a Gaussian structuring element whose standard deviation σ'_i is a function of the distance ρ_i from the support center of the filter: $\sigma'_i = \sigma_0 + \alpha\rho_i$. The parameters σ_0 and α regulate the tolerance to deformation of the concerned DoG positions.

We then *shift* each blurred feature map $C_i(x, y)$ by a distance ρ_i opposite to ϕ_i . In this way all blurred responses at the points of interest meet at the support center of the *B-COSFIRE* filter. For the i -th tuple, we obtain a blurred and shifted feature map $s_i(x, y)$, defined as:

$$s_i(x, y) \triangleq \max_{(x', y') \in \Lambda_i} \{C_i(x - x' + \Delta x, y - y' + \Delta y) G_{\sigma'_i}(x', y')\} \quad (4)$$

where $\Lambda_i = [-3\sigma'_i, 3\sigma'_i] \times [-3\sigma'_i, 3\sigma'_i]$ is the size of the Gaussian structuring element, and $(\Delta x, \Delta y) = (\rho_i \cos \phi_i, -\rho_i \sin \phi_i)$ is the shift vector of the i -th blurred feature map with respect to the support center of the filter.

Finally, we compute the response of a *B-COSFIRE* filter by combining the blurred and shifted feature maps by geometric mean:

$$r_B(x, y) = \left[\prod_{i=1}^{|B|} s_i(x, y) \right]^{1/|B|} \quad (5)$$

B. RUSTICO

The proposed operator uses as input the responses of *B-COSFIRE* filters, with the addition of a novel inhibitory component. This component involves using DoG filters with opposite polarity (i.e. $-\delta_i$) to the excitatory ones and when combined together provide inhibitory input to RUSTICO. With this type of inhibition, areas dominated by noise evoke very similar excitatory and inhibitory responses that cancel each other. We denote by \hat{B}_λ the novel inhibitory component and obtain it by manipulating the parameters of the excitatory component B , as follows:

$$\hat{B}_\lambda \triangleq \{(-\delta, \lambda\sigma_i, \rho_i, \phi), \forall (\delta, \sigma_i, \rho_i, \phi_i) \in B\} \quad (6)$$

The two components differ in two main aspects. They have tuples with opposite polarities and the sizes of the contributing DoG filters in the inhibitory part \hat{B}_λ are multiples of a given λ value ($\lambda > 0$) with respect to their corresponding DoG filters in the excitatory part.

We define RUSTICO as a pair $P_\lambda(B, \hat{B}_\lambda)$ of excitatory and inhibitory components that take input from DoG filters

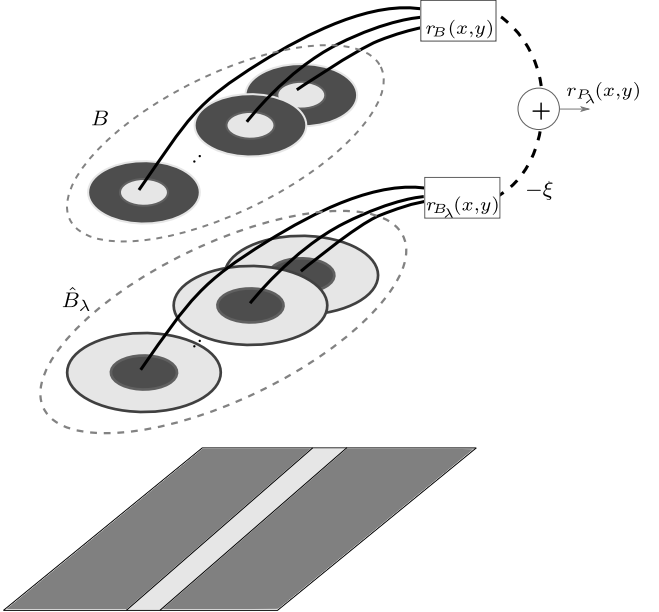


Fig. 3. Augmented view of the structure of the proposed RUSTICO applied to an image of a bright line on dark background. The concentric circles represent the input DoG filters. The set \hat{B}_λ groups the DoG filters of the inhibitory component (center-off), whose sizes are λ times larger than those of their excitatory (center-on) counterparts in the set B . The output of RUSTICO is computed by subtracting the inhibitory response weighted by a given weight ξ , from the excitatory response.

of opposite polarity. We compute its response $r_{P_\lambda}(x, y)$ by subtracting a factor ξ of the inhibitory response $r_{\hat{B}_\lambda}(x, y)$ from the excitatory one, followed by a *ReLU* operation:

$$r_{P_\lambda}(x, y) = \left| r_B(x, y) - \xi r_{\hat{B}_\lambda}(x, y) \right|^+ \quad (7)$$

where the parameter $\xi > 0$ is the inhibition strength, which controls how much of the excitatory response is suppressed.

In Fig. 3, we illustrate a layered sketch of the structure of RUSTICO along with a preferred synthetic pattern with a bright line surrounded by dark background. The excitatory component B is composed of a set of center-on DoG filters. The inhibitory component \hat{B}_λ is composed of center-off DoG filters with supports that are λ times bigger than those of their excitatory counterparts. We compute the RUSTICO response by combining the intermediate excitatory and inhibitory response maps by a linear function $r_{P_\lambda}(x, y)$.

C. Motivation of the λ and ξ Parameters

There is neurophysiological evidence that many simple cells that exhibit push-pull behavior have the orientation bandwidth of the inhibitory (pull) interneuron broader than that of the excitatory (push) neuron [39], [48]. We implement this phenomenon by employing DoG functions with larger supports in the pull unit. The orientation bandwidth of the pull unit increases with an increasing value of the parameter λ . This implementation allows the design of RUSTICO that achieves the same response maps to the noiseless pattern (Fig. 4a) when applied with and without inhibition. In Fig. 4b we show the response map of the excitatory component of RUSTICO to the stimulus in Fig. 4a. In the second row, we show the response maps of the inhibitory component configured with different

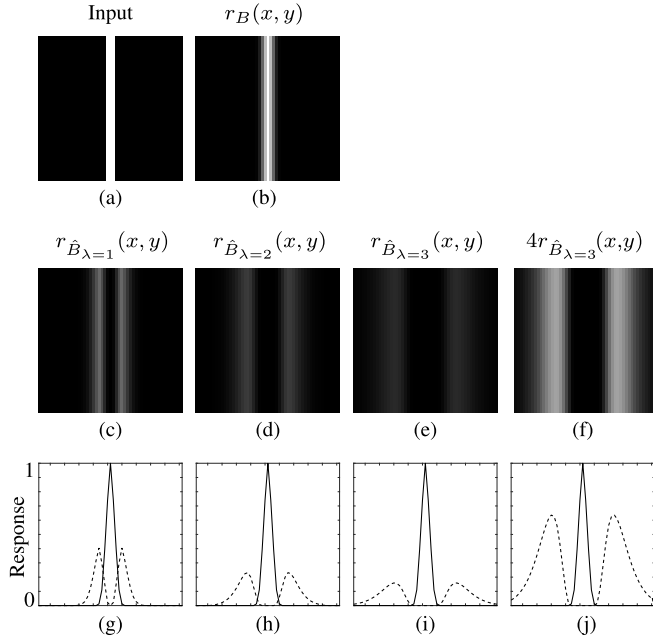


Fig. 4. Behavior of the push and pull units to (a) a synthetic input pattern of size 50×50 pixels with a vertical bar of width 5 pixels. (b) The push responses and (c-f) the pull responses with different values of λ and ξ . (g-j) The response profiles along the central horizontal axis of both push (solid lines) and pull (dashed lines) units. For small values of λ the pull and push responses overlap along the pattern of interest. The pull response profile in (j) is multiplied by $\xi = 4$.

values of the parameters λ and ξ , while the third row illustrates the 1-D profiles of the excitatory and inhibitory responses along the central horizontal row.

In the concerned example, when $\lambda = 1$, the **pull component responds also along the internal sides of the signal** and as a result it, **undesirably, suppresses the push response** (Fig. 4c,g). When $\lambda = 2$, the inhibitory response is much less prominent along the sides of the concerned stimulus (Fig. 4d,h) and when we set $\lambda = 3$ the push and pull responses do not overlap each other, Fig. 4(e,i), thus achieving the desired property.

In Fig. 4(g-i), we can observe that, while the desired property is achieved by using a larger standard deviation for the inhibitory component, the inhibitory responses decrease with an increasing standard deviation. We use the inhibition factor ξ to **compensate** for this effect. The response profile in Fig. 4j shows how we can amplify the pull responses by multiplying them with a high value of ξ , while avoiding any overlap with the push responses. The values of the parameters λ and ξ depend on the application at hand and the amount of noise contained in the images.

D. Intensity and Orientation Maps

The operator that we configured above is selective for vertical vessel-like structures, similar to the prototype used in Fig. 2a. Orientation selectivity can be controlled by **manipulating** the angular parameter values ϕ_i . For a given orientation ψ we can define a new RUSTICO $P_\lambda^\Psi(B^\psi, \hat{B}_\lambda^\psi)$ where the excitatory B^ψ and inhibitory \hat{B}_λ^ψ inputs are defined as:

$$B^\psi = \{(\delta, \sigma_i, \rho_i, \phi_i + \psi), \forall (\delta, \sigma_i, \rho_i, \phi_i) \in B\} \quad (8)$$

$$\hat{B}_\lambda^\psi = \{(-\delta, \lambda\sigma_i, \rho_i, \phi_i + \psi), \forall (-\delta, \lambda\sigma_i, \rho_i, \phi_i) \in \hat{B}_\lambda\} \quad (9)$$

Given a set $\Psi = \{\frac{2\pi}{n_\phi}i \mid i = 1, \dots, n_\phi - 1\}$ of n_ϕ preferred orientations, we define a rotation-tolerant RUSTICO as a set $P_\lambda^\Psi = \{(B^{\psi_i}, \hat{B}_\lambda^{\psi_i}) \mid \psi_i \in \Psi\}$, where each pair $(B^{\psi_i}, \hat{B}_\lambda^{\psi_i})$ is a RUSTICO with orientation preference ψ_i .

The response of a rotation-tolerant RUSTICO consists of an intensity map $\hat{RI}_\lambda^\Psi(x, y)$ and an orientation map $\hat{RO}_\lambda^\Psi(x, y)$, which we define as follows:

$$\hat{RI}_\lambda^\Psi(x, y) \triangleq \max_{\psi \in \Psi} \{|r_{B^{\psi_i}}(x, y) - \xi r_{\hat{B}_\lambda^{\psi_i}}(x, y)|^+\} \quad (10)$$

$$\hat{RO}_\lambda^\Psi(x, y) \triangleq \begin{cases} \operatorname{argmax}_{\psi \in \Psi} \{|r_{B^{\psi_i}}(x, y) - \xi r_{\hat{B}_\lambda^{\psi_i}}(x, y)|^+\}, & \hat{RI}_\lambda^\Psi(x, y) > 0 \\ \text{NaN} & \text{otherwise} \end{cases} \quad (11)$$

The intensity map \hat{RI}_λ^Ψ indicates the curvilinearity degree of each pixel in the given image, while the orientation map \hat{RO}_λ^Ψ represents their discretized orientations. For each location whose intensity value is zero we assign to it a *not a number* (NaN) value in the orientation map.

IV. ROBUSTNESS TO NOISE AND CURVATURES

In this section, we report the results that we achieved by comparing the performance of RUSTICO with that of the B-COSFIRE filter on synthetic images only. The purpose of this analysis is to study, **under controlled conditions**, the contribution of the proposed inhibitory component to the improvement of delineation results when noise of different types and levels or **high curvature points** are present in the images. For results on benchmark data sets of real-world images and comparison with existing methods, we refer the reader to Section VI.

A. Synthetic Lines With Added Noise

We created a synthetic data set of vertical line images of size 50×50 pixels with four types of noise, namely **Gaussian, Rician, Poisson and bandlimited**. The former three types of noise are typically found in medical images, such X-rays, magnetic resonance and retinal fundus, or introduced by camera sensors, while bandlimited noise has been shown to suppress **visual perception of stimuli** [49].

For Gaussian and Rician noise we generate stimuli with 10 values of standard deviation that vary from 0.1 to 1 in steps of 0.1. Poisson noise is a function of the intensity pixels and valid Poisson distributions can be generated with mean (i.e. intensity value) > 0 . For these experiments we change the contrast between the line signal and the background such that the background pixels are not zeros. We consider five levels of contrasts (0.031, 0.063, 0.125, 0.25, 0.5), where each contrast value indicates the background intensity. For the bandlimited noise experiments we first generate noisy stimuli with 10 frequencies between 1 and 10 in steps of 1 and add the line signal in the center with five contrast levels (0.031, 0.063, 0.125, 0.25, 0.5).

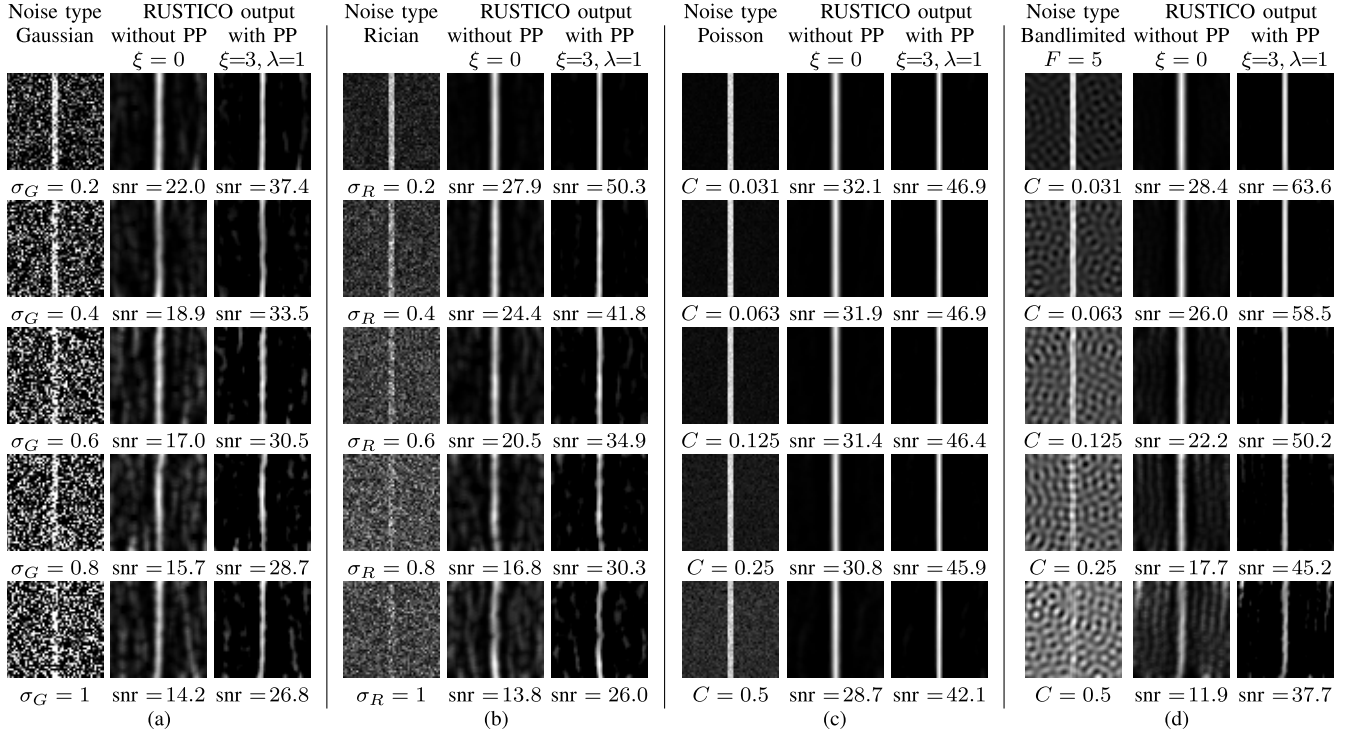


Fig. 5. Evaluation of RUSTICO without ($\xi = 0$) and with ($\xi = 3$) push-pull (PP) inhibition on synthetic images with different types of noise: (a) Gaussian, (b) Rician, (c) Poisson and (d) bandlimited. The signal-to-noise ratio (snr) of the response maps achieved by RUSTICO with inhibition is consistently better than the excitatory-only RUSTICO. The parameters σ_G and σ_R are the standard deviations of Gaussian and Rician noise, respectively. The parameter C in (c) and (d) indicates the contrast between the stimulus and the background. The parameter F in (d) represents the frequency of the bandlimited noise.

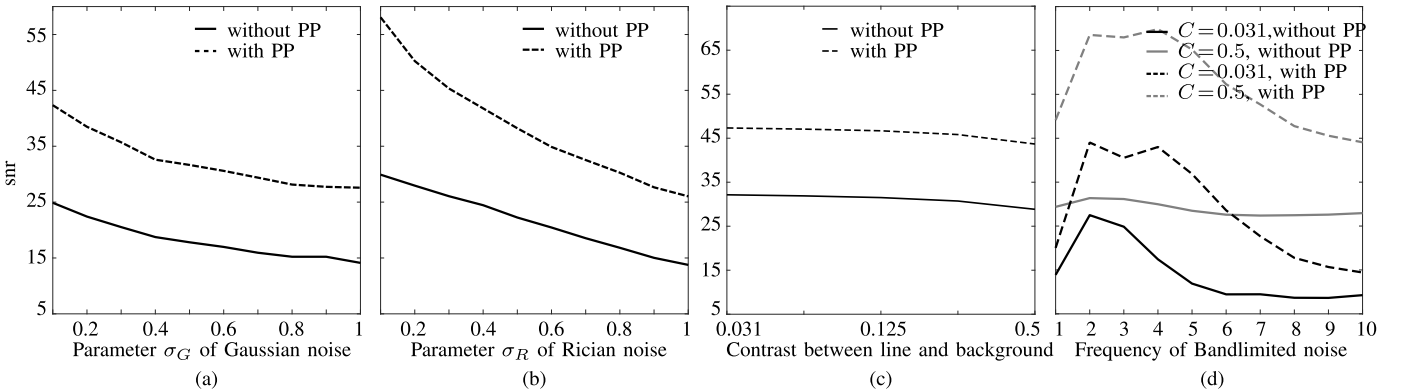


Fig. 6. Performance of RUSTICO with ($\xi = 3, \lambda = 1$) and without ($\xi = 0$) push-pull (PP) inhibition on line stimuli with four different types of noise: (a) Gaussian, (b) Rician, (c) Poisson and (d) bandlimited. The parameter c in (d) indicates the contrast between the line and the background.

For each noisy image we apply RUSTICO with ($\xi > 0$) and without ($\xi = 0$) inhibition, and compute the signal-to-noise ratio (snr) on both output images as:

$$snr = 20 \log_{10}(A_S/A_B) \quad (12)$$

where A_S is the mean response along the line pattern and A_B is the mean response in the background.

In order to compensate for the randomness of noise, we generate 20 noisy stimuli with the same parameters and take the mean snr of the resulting output images. In Fig. 5, we show some examples from the created synthetic data set. The output images generated by RUSTICO with push-pull inhibition exhibit consistent improvement of snr. Fig. 6

illustrates this significant improvement over varying values of the involved parameters for each type of added noise.

B. Synthetic Dashed and Curved Patterns With Noise

We studied the robustness of RUSTICO with respect to lines with high curvature degree and to occlusions (e.g. dashed lines) when the four types of noise mentioned above are present in the images. For each image in the first row of Fig. 7, we apply RUSTICO with and without inhibition and illustrate the best resulting binary maps according to the CAL measurement (for details on the CAL metric, please refer to Section VI-B). Also in these experiments, the inhibitory component introduced in RUSTICO makes the operator more

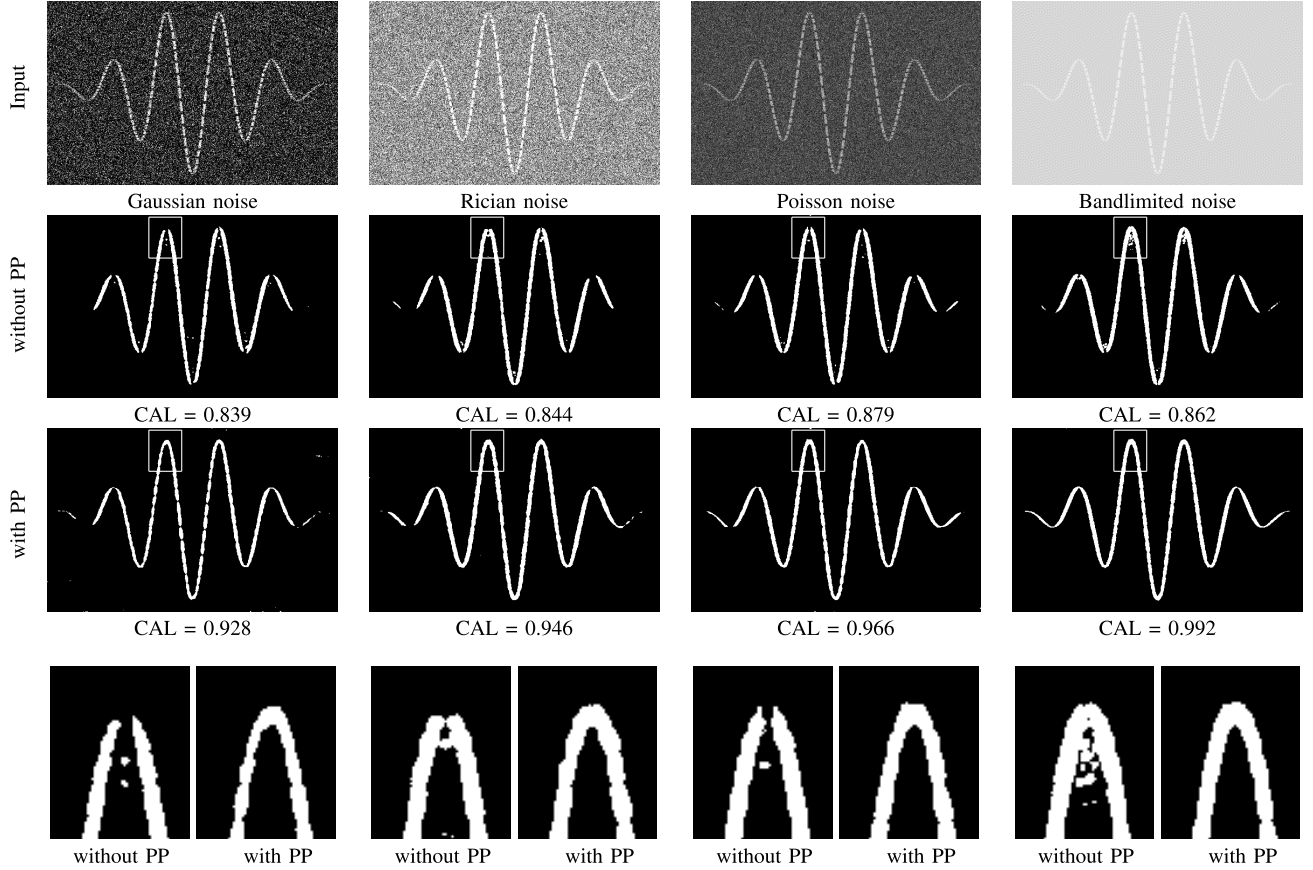


Fig. 7. Evaluation of RUSTICO with push-pull inhibition ($\lambda = 3, \xi = 2$) in contrast to the original B-COSFIRE filter with respect to (first row) four noisy dashed lines with a mix of high and low curvatures. The second and third rows show the resulting binary maps with the highest CAL values (see Section VI-B for details about the CAL metric). In the fourth row, we compare a detail (zoomed-in views of the enframed areas in the second and third row) of the segmentation obtained with and without the push-pull inhibition component. In all cases, the inhibition improves the robustness to noise and preserves better the smoothness in high-curvature points.

robust to noise and preserves better the smoothness of the lines in points of high curvature. In the fourth row of Fig. 7, we include the zoomed-in views of the enframed areas in the images given in the second and third row. These images show the same of the response map of the B-COSFIRE filter and RUSTICO around a point of high curvature in presence of noise. In all cases, RUSTICO with a push-pull inhibitory component achieves much better results in such salient points than without inhibition. RUSTICO is also more robust to the ending parts of the synthetic patterns.

V. DATA

We investigate the effectiveness of RUSTICO in various applications, namely segmentation of rivers and roads from aerial images, delineation of blood vessels in retinal images, detection of rose stems for gardening robotics, and pavement crack detection. We carried out experiments on several benchmark data sets, for which we provide details below.

A. Aerial Road and River Images

We consider two aerial images of a road network and a river released in [8], of size 894×650 and 364×320 pixels, respectively. The images contain noise and artifacts, which

make the segmentation process very challenging. Ground truth images are provided in the form of binary maps.

B. Retinal Fundus Images

We used the following four data sets: STARE [25], DRIVE [14], CHASE_DB1 [50] and HRF [51].

The STARE data set is composed of 20 images (of size 700×605 pixels), half of which contain signs of pathology. All images are accompanied by manually segmented images of the vessel trees provided by two observers.

The DRIVE data set contains 40 images, divided in 20 images for training and 20 for testing (of size 768×584 pixels). Each image is distributed together with a mask of the field of view (FOV) of the retina. The images in the training set were manually segmented by a single observer, while those in the test set were segmented by two observers.

The CHASE_DB1 data set contains 28 images (of size 999×960 pixels) from both eyes of 14 patients in the program “Child Heart And Health Study in England”. Each image was manually segmented by two observers.

For the STARE, DRIVE and CHASE_DB1 data sets, we use the ground truth of the first observer as gold standard.

The HRF data set contains 45 images with a resolution of 3504×2336 pixels, which is substantially higher than the

images of the other data sets. It is composed of three sets of 15 images collected from healthy people, patients with glaucoma and with diabetic retinopathy. Each image has one manually segmented ground truth of the vessel tree.

C. Rose Stems

We created a data set of 35 images of rose bushes, named TB-roses35, for which we provide binary maps with manually segmented rose stems that serve as ground truth. The data set is publicly available.¹ Analysis of this kind of images is important, for instance, for automatic detection and segmentation of rose stems, which is a basic step for applications of visual-servoed robotics for plant cutting. The images are of size 720×540 pixels and were recorded in the test garden of the EU TrimBot2020 project [52] at Wageningen University and Research campus. This data set contributes to extending the benchmark of delineation and segmentation algorithms and their performance analysis to outdoor and highly textured environments (e.g. gardens).

D. Pavement Cracks

We carried out experiments on three data sets of pavement cracks, namely the Crack_pv14 [53], the Crack_ivc [54] and the CrackTree206 [55]. The Crack_ivc and CrackTree206 data sets are composed of 5 and 206 RGB images of cracked asphalt of size 512×512 pixels and 800×600 pixels, respectively. The Crack_pv14 data set is composed of 14 images of road cracks taken with a laser range imaging appliance, mounted on the back of a car [53]. The images have resolutions of 200×300 pixels. The three data sets contain manually annotated ground truth images, which consist in one-pixel wide contours that indicate the center-lines of the cracks.

VI. EXPERIMENTAL EVALUATION

A. Experimental Pipelines

We employ RUSTICO in different image processing pipelines, designed according to the characteristics and requirements of the applications at hand. In this work we demonstrate that the proposed method can be effectively combined with other techniques to solve various tasks. We publicly provide a MATLAB implementation of the employed processing pipelines.

1) Aerial Image Processing: For the problems of segmentation of rose stems and extraction of roads and rivers from aerial images, we directly process the input images with RUSTICO without any preprocessing. We obtain the final binary image by thresholding the output map of RUSTICO.

2) Retinal Vessel Segmentation: In retinal fundus images, the highest contrast between vessels and background is in the green channel of the RGB color space [28]. In order to avoid false detection of vessels along the border of the retinal field of view (FOV), we apply an iterative procedure to enlarge the FOV, by increasing the radius of its outer border. For further details, we refer the reader to [13]. We then apply the contrast-limited adaptive histogram equalization (CLAHE)

algorithm, which improves the local contrast by avoiding over-amplification of noise in homogeneous regions. We process the output of the CLAHE algorithm with RUSTICO and obtain a binary vessel map by thresholding its response map.

3) Rose Stem and Crack Delineation: We apply the processing pipeline proposed in [56], where we substitute the B-COSFIRE filter with RUSTICO. We process the RUSTICO intensity and orientation output maps by thinning, hysteresis thresholding and morphological closing, in order to obtain the center-line of the detected cracks.

B. Performance Evaluation

We apply two performance evaluation procedures according to the requirements of the concerned applications, one for roads, rivers and blood vessel segmentation, while the other one for rose stems and crack delineation.

1) Road, Rivers, Blood Vessel Segmentation: We threshold the responses of RUSTICO and obtain a binary map that we compare with the corresponding ground truth image. We compute the Matthews correlation coefficient (MCC), which is a suitable measurement of the accuracy of binary classification in the case of unbalanced classes [57]. The MCC has been widely used for evaluation of image segmentation algorithms [32], [58], [59]. We chose the MCC as, in the considered applications, the background (negative) pixels outnumber the foreground (positive) pixels, which produce a bias effect on the accuracy, specificity and sensitivity. The MCC is defined as:

$$MCC = \frac{TP/N - S \cdot P}{\sqrt{P \cdot S \cdot (1 - S) \cdot (1 - P)}},$$

where TP is the number of true positives, FP false positives, TN true negatives, FN false negatives, $N = TN + TP + FN + FP$, $S = (TP + FN)/N$ and $P = (TP + FP)/N$.

The MCC is computed by comparing the segmentation output with the corresponding ground truth image in a pixel-to-pixel manner. This kind of evaluation is strictly dependent on the specific ground truth provided by a human observer. Furthermore, human observers are not always able to sharply detect the right position of line boundaries [60], resulting in different ground truths provided by different observers.

For an extensive evaluation of the quality of segmentation we employ the assessment metric proposed in [61]. Instead of performing a pixel-to-pixel comparison, this metric takes into account certain properties of line networks by computing three measures of connectivity, area and length. It has been demonstrated to have high matching degree with human quality perception and to be robust to ground truth images provided by different observers. Let I_S be the obtained segmented image and I_G the corresponding ground truth image. The considered metric evaluates:

- *Connectivity (C).* It measures the fragmentation degree of I_S with respect to the ground truth I_G and penalizes fragmented segmentation. It is defined as:

$$C(I_S, I_G) = 1 - \min \left(1, \frac{|\#_C(I_G) - \#_C(I_S)|}{\#(I_G)} \right)$$

¹The data set is available at the url <http://gitlab.com/nicstrisc/RUSTICO>

where $\#_C(\cdot)$ counts the connected components, while $\#(\cdot)$ computes the number of foreground pixels in the considered binary image.

- *Area (A)*. It evaluates the overlapping area between I_S and I_G , based on the Jaccard coefficient. Let $\delta_\varepsilon(\cdot)$ be a morphological dilation that uses a disc structuring element with a radius of ε pixels. The measure A is defined as follows:

$$A(I_S, I_G) = \frac{\#((\delta_\varepsilon(I_S) \cap I_G) \cup (I_S \cap \delta_\varepsilon(I_G)))}{\#(I_G \cup I_S)}$$

The value of ε controls the tolerance to lines of different widths. We set $\varepsilon = 2$.

- *Length (L)*. It evaluates the matching degree between I_S and I_G by measuring the length of the two line networks:

$$L(I_S, I_G) = \frac{\#((\varphi(I_S) \cap \delta_\beta(I_G)) \cup (\delta_\beta(I_S) \cap \varphi(I_G)))}{\#(\varphi(I_S) \cup \varphi(I_G))}$$

where $\varphi(\cdot)$ is a skeletonization operation and $\delta_\beta(\cdot)$ is a morphological dilation with a disc structuring element of β pixels radius. The value of β controls the tolerance to variations of the line tracing output. We set $\beta = 2$.

The final evaluation metric, named CAL , is defined as $f(C, A, L) = C \cdot A \cdot L$.

For each image in a given data set we binarize the output map of RUSTICO by varying the threshold t from 0 to 1 in steps of 0.01, and compute the MCC and CAL values for every binarized output image. Then, for every threshold value, we compute the average MCC , denoted by \overline{MCC} , and the average CAL , denoted by \overline{CAL} , values across the binary outputs of all images in the data set, and choose the threshold t^* that contributes to the maximum \overline{CAL} value.

2) *Rose Stem and Crack Detection*: For rose stem and pavement crack detection, we adopt the evaluation protocol proposed in [55], which takes into account precision (Pr), recall (Re) and F-measure (F):

$$Pr = \frac{TP}{TP + FP}, Re = \frac{TP}{TP + FN}, F = \frac{2 \cdot Pr \cdot Re}{Pr + Re} \quad (13)$$

According to [53], [55], for the computation of the performance measures we take into account a certain tolerance to compensate for some imprecision in the ground truth. If a crack pixel is detected not farther than d^* pixels from the nearest ground truth pixel, it is considered as a TP, otherwise it is a FP. For each image we compute the three metrics in Eq. 13 for values of the threshold t from 0 to 1 in steps of 0.01. We select the threshold t^* that contributes to the highest average F-measure \bar{F} on the considered data set. We also compute the Precision-Recall curve, which gives a broader understanding of the overall classification performance. The curve is constructed by computing the values of precision and recall for each threshold t .

C. Results and Comparison

The push-pull inhibitory component that we introduced in RUSTICO contributes to the improvement of segmentation results with high statistical significance. In the following, we present the results of a large quantitative evaluation that we performed on the mentioned benchmark data sets.

TABLE I

RESULTS ACHIEVED BY RUSTICO IN COMPARISON WITH THOSE OBTAINED BY *B-COSFIRE* FILTERS ON THE CONSIDERED DATA SETS. THE NUMBER OF IMAGES CONTAINED IN EACH DATA SET ARE REPORTED IN THE SECOND COLUMN, WHILE THE *p*-VALUES OF THE RIGHT-TAILED *t*-TEST STATISTICS IN THE LAST COLUMN. BOLD VALUES INDICATE THAT THE RESULTS ACHIEVED BY RUSTICO ARE STATISTICALLY HIGHER THAN THOSE OF *B-COSFIRE*. THE ROAD AND RIVER AERIAL IMAGES ARE SINGLE EXAMPLES AND, HENCE, *t*-TEST STATISTICS ARE NOT APPLICABLE

Dataset	No. of images	Method	Results	
			CAL	<i>p</i>
Road	1	<i>B-COSFIRE</i>	0.6091	n/a
		RUSTICO	0.6343	
River	1	<i>B-COSFIRE</i>	0.4397	-
		RUSTICO	0.6523	
STARE	20	<i>B-COSFIRE</i>	0.6976	-
		RUSTICO	0.6976	
DRIVE	20	<i>B-COSFIRE</i>	0.7213	< 0.05
		RUSTICO	0.7280	
CHASE_DB1	28	<i>B-COSFIRE</i>	0.6084	-
		RUSTICO	0.6202	
HRF	45	<i>B-COSFIRE</i>	0.5678	< 0.01
		RUSTICO	0.5774	
F-score				
TB-roses	35	<i>B-COSFIRE</i>	0.3385	-
		RUSTICO	0.3822	
Crack_ivc	5	<i>B-COSFIRE</i>	0.7728	< 0.05
		RUSTICO	0.8299	
CrackTree206	206	<i>B-COSFIRE</i>	0.6630	-
		RUSTICO	0.6846	
Crack_pv14	14	<i>B-COSFIRE</i>	0.9173	< 0.05
		RUSTICO	0.9199	

We report the performance results achieved by RUSTICO and compare them with the ones obtained by the *B-COSFIRE* filter in Table I. The values of CAL are computed after thresholding the response maps of RUSTICO and *B-COSFIRE* according to the criteria described in Section VI-B. The improvement of the CAL metric with respect to the results achieved by the *B-COSFIRE* filter is statistically significant on most of the considered data sets. As a matter of fact, on the DRIVE, CHASE_DB1 and HRF, TB-roses35, Crack_ivc, CrackTree206 and Crack_pv14 data sets, the significance of the performance improvement is confirmed by the right-tailed paired *t*-test statistics (DRIVE: $p < 0.05$; CHASE_DB1: $p < 0.01$, HRF: $p < 0.01$; TB-roses35: $p < 0.01$; Crack_ivc: $p < 0.05$; CrackTree206: $p < 0.01$; Crack_pv14: $p < 0.05$). The road and river aerial images are single examples and, hence, statistical analysis is not applicable. It is noticeable that for the STARE data set, the push-pull inhibition component of RUSTICO does not contribute to an improvement of performance with respect to the *B-COSFIRE* approach. This is mainly due to the characteristics of the STARE data set, whose images do not contain large amount of noise and texture in the background. RUSTICO significantly

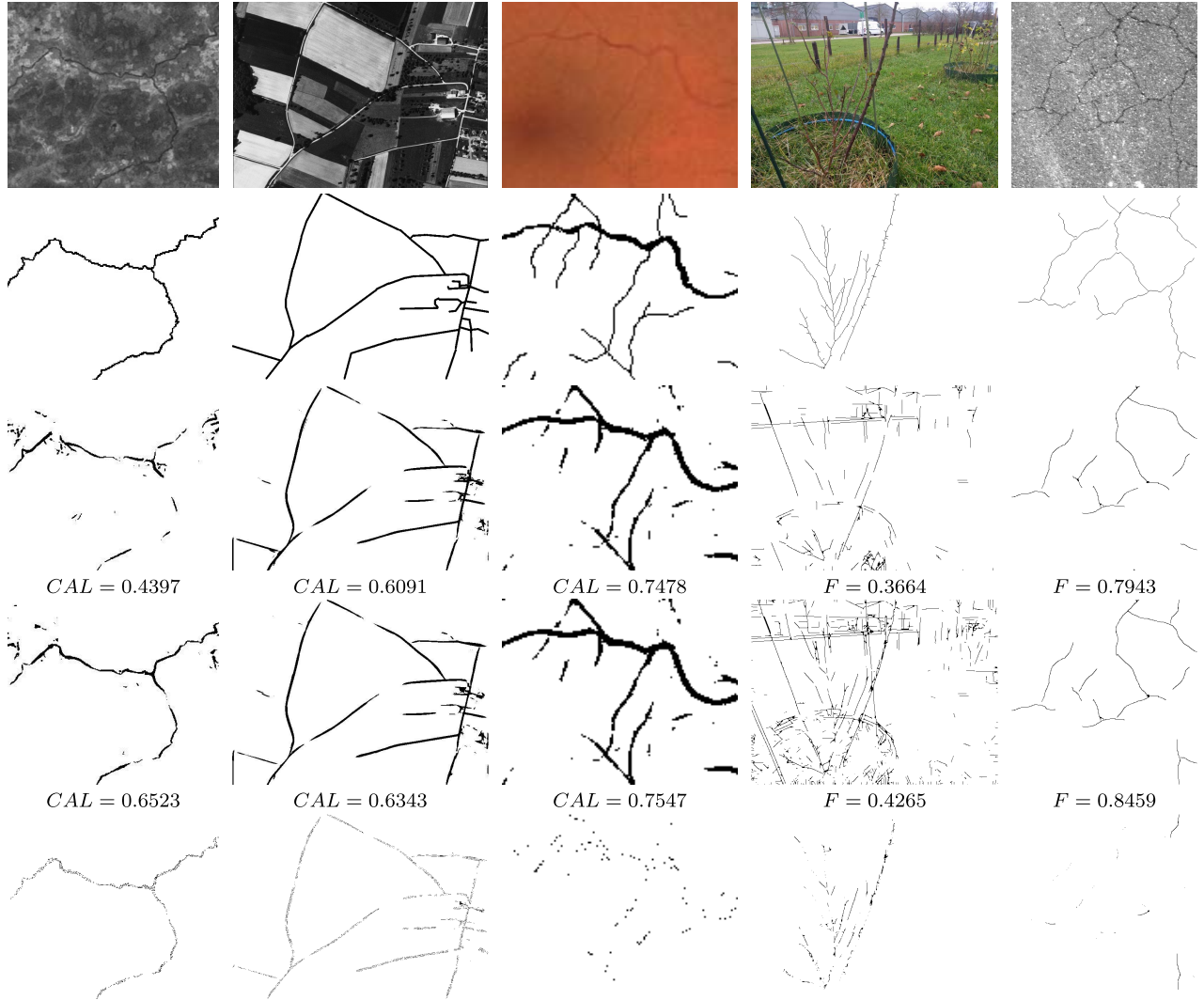


Fig. 8. (First row) Example images from the considered data sets, together with (second row) their corresponding ground truth images. The third and fourth rows illustrate the delineations obtained by *B-COSFIRE* and *RUSTICO* together with the value of the performance metrics, respectively. The fifth row illustrates the parts of the structures of interest that are detected by *RUSTICO* and missed by *B-COSFIRE*.

outperforms *B-COSFIRE* filters for the detection of rose stems, although most of the errors are caused by the detection of curvilinear and elongated structures that are not part of rose bushes (e.g. poles). *RUSTICO* is, thus, able to detect very fine structures also in very hard situations where noise and texture are present in the images.

In Fig. 8, we show example images and segmented output maps obtained by *RUSTICO* (fourth row) in comparison with the outputs obtained using the *B-COSFIRE* filters (third row). The proposed operator is more effective than *B-COSFIRE* filters, achieving generally higher values of the *CAL* metric and *F*-measure. The improvement of the quality of the delineation output is illustrated in the images in the fifth row of Fig. 8, where we show the parts of the structures of interest that are detected by *RUSTICO* and not detected by *B-COSFIRE*. This is also evident from the quantitative results that we report for the images in Fig. 8. For example, on the river image *RUSTICO* achieves a *CAL* value of 0.6523, which is much higher than the value of 0.4397 obtained by *B-COSFIRE*.

In Table II, we compare the results of *RUSTICO* for the segmentation of vessels in retinal images with those of other approaches on the DRIVE and STARE data sets. We report the results of unsupervised approaches above the dashed lines, while the results of supervised approaches below the dashed lines. We computed the *MCC* and *CAL* values of existing methods using the segmented images that the authors made publicly available. For RORPO [35], we carried out experiments using the implementation provided by the authors and fine-tuned its parameters by a grid search. For methods that achieved statistically significant lower results than *RUSTICO*, we report the significance level of a right-tailed paired *t*-test statistic. The sign - indicates that there is no statistical difference between the results of *RUSTICO* and the corresponding method. The signs * and ** indicate that the corresponding method achieved statistically higher results than those of *RUSTICO* with significance levels of 0.05 and 0.01, respectively. For the DRIVE data set, the average *CAL* achieved by the proposed operator is statistically

TABLE II

COMPARISON OF RESULTS OF RUSTICO WITH THE ONES OF EXISTING APPROACHES ON RETINAL IMAGES. THE METHODS ABOVE THE DASHED LINES ARE UNSUPERVISED WHILE THE ONES BELOW ARE SUPERVISED. THE SIGN - INDICATES THAT THE RESULTS OF THE CORRESPONDING APPROACHES ARE NOT STATISTICALLY DIFFERENT THAN THOSE OF RUSTICO. THE * AND ** SIGNS INDICATE AVERAGE RESULTS STATISTICALLY HIGHER THAN THE ONES OBTAINED BY RUSTICO WITH SIGNIFICANCE LEVELS OF 0.05 AND 0.01, RESPECTIVELY

Results comparison on the DRIVE data set

Method	MCC	p	CAL	p
RUSTICO	0.7287	-	0.7280	-
<i>B</i> -COSFIRE [32]	0.7189	< 0.01	0.7213	< 0.05
Chauduri <i>et al.</i> [62]	0.4197	< 0.01	0.2075	< 0.01
Jiang <i>et al.</i> [63]	0.6378	< 0.01	0.5178	< 0.01
Perez <i>et al.</i> [29]	0.6645	< 0.05	0.5673	< 0.01
Zana <i>et al.</i> [27]	0.7258	-	0.6180	< 0.01
RORPO [35]	0.6871	< 0.01	0.6228	< 0.01
Niemeijer <i>et al.</i> [12]	0.7222	-	0.6589	< 0.01
Staal <i>et al.</i> [14]	0.7378	*	0.7010	< 0.05
Orlando <i>et al.</i> [64]	0.7482	**	0.7283	-
FC-CRF [65]	0.7556	**	0.7311	-
UP-CRF [65]	0.7401	*	0.6747	< 0.01

Results comparison on the STARE data set

Method	MCC	p	CAL	p
RUSTICO	0.6976	-	0.7087	-
<i>B</i> -COSFIRE [32]	0.6976	-	0.7087	-
Hoover <i>et al.</i> [25]	0.6147	< 0.01	0.5341	< 0.01
RORPO [35]	0.6409	< 0.01	0.5744	< 0.01
FC-CRF [65]	0.7271	-	0.6581	-
UP-CRF [65]	0.7265	-	0.6649	-
U-Net [17]	0.7878	**	0.7605	**

Results comparison on the CHASE_DB1 data set

Method	MCC	p	CAL	p
RUSTICO	0.6628	-	0.6202	-
<i>B</i> -COSFIRE [32]	0.6556	< 0.01	0.6084	< 0.01
FC-CRF [65]	0.7039	**	0.6223	-
UP-CRF [65]	0.6888	*	0.5714	-
DeepVessel [66]	0.7059	**	0.6824	**

Results comparison on the HRF data set

Method	MCC	p	CAL	p
RUSTICO	0.6905	-	0.5874	-
<i>B</i> -COSFIRE [32]	0.6858	< 0.01	0.5771	< 0.01
FC-CRF [65]	0.6901	-	0.5409	< 0.01
UP-CRF [65]	0.6775	< 0.01	0.4751	< 0.01

higher than those obtained by many existing approaches, as confirmed by the *p*-values that we report in Table II. The methods proposed by Orlando and Blaschko [64] and Orlando *et al.* [65], based on Fully Connected Conditional Random Fields (FC-CRF), achieved comparable values of CAL to that of RUSTICO on the DRIVE, STARE and CHASE_DB1 data sets and a significantly lower value of CAL on the HRF data set of high resolution images.. The MCC

TABLE III

COMPARISON OF PERFORMANCE RESULTS ACHIEVED TWO AERIAL IMAGES, ONE DEPICTING A ROAD AND THE OTHER ONE A RIVER. THE METHODS ARE ALL UNSUPERVISED

Method	Road		River	
	MCC	CAL	MCC	CAL
RUSTICO	0.6859	0.6343	0.5719	0.6523
<i>B</i> -COSFIRE	0.6761	0.6091	0.4771	0.4397
Verdie <i>et al.</i> [7]	0.7413	0.6116	0.5542	0.5981
Lafarge <i>et al.</i> [8]	0.6651	0.4554	0.4982	0.5274
Lacoste <i>et al.</i> [6]	0.8302	0.7538	0.6419	0.8146
Rochery <i>et al.</i> [67]	0.5427	0.3632	0.5073	0.4795
RORPO [35]	0.4728	0.4230	0.4746	0.5008

achieved by RUSTICO is higher than the one obtained by other methods based on filtering (i.e. unsupervised) approaches, while it is statistically lower than the supervised methods (i.e. based on machine learning techniques) proposed in [64], [65] and in [14], with significance level of 0.01 and 0.05, respectively. The results that we achieved on the STARE data set are statistically higher than or comparable to the ones obtained by other approaches, both in terms of MCC and CAL. Only the U-Net convolutional neural network [17] and DeepVessel [66], achieve statistically higher values of MCC and CAL ($p < 0.01$). For the evaluation on the HRF data set, we compute the results for 30 images out of 45, as the first 15 images are used by Orlando *et al.* [65] to train the UP-CRF and FC-CRF models. It is noticeable how on high-resolution images contained in the HRF data set, RUSTICO achieves a statistically higher value of CAL than the more complex FC-CRF and UP-CRF approaches.

RUSTICO is a general approach for delineation of curvilinear patterns in unsupervised way, while the methods we compared with are specifically tailored or fine-tuned (e.g. U-Net, which is adapted to vessel segmentation while the original architecture is designed for cell segmentation) for the delineation of blood vessels in retinal fundus images. The only other method that is designed as an operator general curvilinear pattern detection is RORPO, which achieved much lower results than RUSTICO. Notable is the fact that the RUSTICO that we employed in the experiments is a single operator and it is not directly comparable with machine learning based approaches and CNNs, which employ hundreds or thousands of filters organized in a hierarchical fashion, e.g. U-Net and DeepVessel.

In Table III, we report the MCC and CAL values achieved by RUSTICO and other existing unsupervised methods on the road and river aerial images. RUSTICO outperforms the approaches proposed in [7], [8], [67], and performed less than the method proposed in [6]. These four methods were designed to deal with specific problems of the images at hand and are computationally expensive. In [68], it was reported that they require a processing time that is one to three orders of magnitude higher than the one required by *B*-COSFIRE filters. RUSTICO requires double processing time than *B*-COSFIRE filters, on average. RORPO, which is the only other general

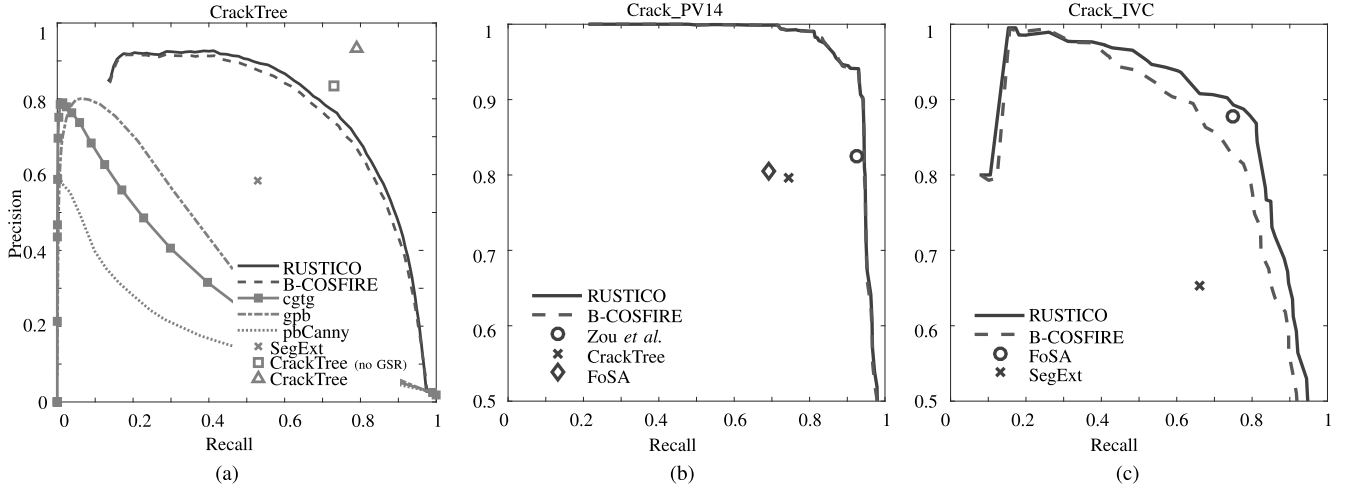


Fig. 9. Precision-Recall curves achieved by RUSTICO (solid line) and *B*-COSFIRE (dashed line) on the (a) Crack_ivc, (b) CrackTree, and (c) Crack_pv14 data sets, together with the results achieved by existing approaches.

approach to delineation of curvilinear structures, achieved much lower results than RUSTICO.

We report the Precision-Recall curves achieved by RUSTICO on the Crack_ivc, CrackTree206 and Crack_pv14 data sets in Figs. 9a, 9b and 9c, respectively. Existing methods, except for the CrackTree [55] algorithm on the CrackTree206 data set, performed less than RUSTICO. In particular, the average *F*-measure of RUSTICO on the Crack_ivc data set ($F = 0.8299$) is higher than those of existing methods (*B*-COSFIRE: $F = 0.7765$; FoSA: $F = 0.7719$; SegExt: 0.6526), as it is shown in Fig. 9b. On the CrackTree206 data set, RUSTICO performed better ($F = 0.6846$) than many existing approaches, namely *B*-COSFIRE ($F = 0.6630$), SegExt [69] ($F = 0.55$), Canny ($F = 0.26$), global pb ($F = 0.44$) and pbCGTG [70] ($F = 0.35$). The results of the CrackTree algorithm, both when a pre-processing step with global shadow removal (GSR) algorithm is used and when it is not used (*F*-measure of 0.85 and 0.77, respectively), are higher than those of RUSTICO. On the Crack_pv14 data set, we obtained an *F*-measure of 0.9199, which is statistically higher than those obtained by Zou *et al.* [55] ($F = 0.8665$, $p < 0.05$), CrackTree ($F = 0.7664$, $p < 0.01$) and FoSA ($F = 0.7380$, $p < 0.01$). Despite of very similar precision-recall curves obtained by *B*-COSFIRE and RUSTICO, we observed that the average *F*-measure achieved by *B*-COSFIRE ($F = 0.9172$) is statistically significantly lower than the one of RUSTICO, with $p < 0.05$.

It is important to highlight that the best performing methods on the considered data sets were designed to deal with specific problems and characteristics of the concerned applications. For instance, the CrackTree and FoSA algorithms were designed for the detection of cracks in RGB images. Their performance drastically drops when they are applied to different kinds of image, even if from the same application, e.g. when they are applied to the laser range images in the Crack_pv14 data set. RUSTICO is, instead, designed as a general approach to segmentation of curvilinear structures and achieves results that

are comparable or, in most cases, higher than those reported in the literature for various applications and image sources.

D. Hyperparameters

The values of the parameters of RUSTICO have to be manually set according to the characteristics of the curvilinear structures of interest and of the particular images analyzed. For instance, the value of σ determines the selectivity of the operator to structures of certain thicknesses (see Section III-A), while the values of λ and ξ regulate the size of the image region in which the noise is suppressed and the strength of suppression, respectively (see Section III-C). For the application of retinal vessel delineation, the images in the STARE and DRIVE data sets have lower resolutions than the images in the CHASE_DB1 and HRF data sets. As a result, the blood vessels in the latter data sets are thicker than the ones in the former data sets. The operators involved in the processing of such images need to be configured with higher values of σ . Similarly, the Crack_pv14 data set contains lower resolution images than those in the Crack_ivc and CrackTree206 data sets, so requiring a smaller value of σ . On the contrary, the larger presence of textured background in the Crack_ivc and CrackTree206 data sets requires higher values of the parameters λ and ξ that regulate the degree of noise suppression.

VII. DISCUSSION AND OUTLOOK

The significant improvement of the performance results achieved by RUSTICO with respect to the *B*-COSFIRE filters and other methods on various benchmark data sets is attributable to the contribution of the newly introduced inhibitory component. In our experiments we demonstrated how RUSTICO is able to suppress responses to noise and spurious texture. As a consequence, structures of interest and their more challenging parts, such as thin and low-contrast ones, are better detected. This is particularly evident from the results achieved on the TB-roses35 data set. RUSTICO is able to detect more challenging parts of the rose stems,

e.g. thin branches in highly textured regions. Most of the detection errors of RUSTICO are, however, caused by elongated structures that are not part of rose bushes, such as window borders and poles. The robustness of RUSTICO to such cases and the quality of the delineation output can be further improved by considering color or depth information. This would contribute to increasing the selectivity of the proposed operator for the patterns of interest. Furthermore, in such cases, RUSTICO can be employed in more complex pipelines and its output can serve as prior for advanced image processing and computer vision algorithms, e.g. scene understanding or semantic segmentation.

We do not aim at comparing the performance of RUSTICO against the results achieved by methods based on deep learning and CNNs, which instead require to process hundreds or even thousands of 3-dimensional convolutions. The response maps of RUSTICO can be used as prior input to CNNs or concatenated to their intermediate response maps to facilitate the learning of representations that are robust to texture and noise, especially along object boundaries.

One point of strength of RUSTICO is that it is a configurable operator, in that its selectivity for patterns of interest is determined by a configuration algorithm that analyses a prototype example rather than being fixed in the implementation. The automatic configuration procedure determines the structure of RUSTICO, i.e. the position (ρ_i, ϕ_i) of its DoG contributing filters with respect to the center of the filter support. The values of other hyperparameters, namely $\sigma, \alpha, \sigma_0, \xi, \lambda$ are to be set by the user according to the guidelines we discussed in Section VI-D and to the constraints of the application at hand. However, automatic procedures to determine the values of these parameters can be employed by using RUSTICO within a supervised learning framework that uses optimization techniques based on genetic algorithms [71], or machine learning and information theory [34], [72].

Configurable (or trainable) operators and feature extractors were previously proposed for object recognition [73], [74], sound event detection [75], [76] and human action recognition [77]. They were also integrated into CNN architectures and applied to object and place recognition [78]. Besides curvilinear structures, RUSTICO can be configured to be selective for other types of pattern, such as corners, T- or Y-junctions, and cross-over lines by presenting examples of such patterns to the configuration algorithm. In the application phase to new images, RUSTICO accounts for tolerance to modifications with respect to the prototype pattern used for configuration and it is able to detect also deformed versions of it, to some extent. For example, the operator configured with the synthetic straight line in Fig. 2a is also able to delineate structures with high degree of curvilinearity (see Fig. 7). The degree of tolerance is regulated by the values of the parameters σ_0 and α . Tolerance increases with increasing values of these parameters.

VIII. CONCLUSIONS

We propose a novel operator for delineation of curvilinear structures, which we call RUSTICO (RobUST Inhibitory-augmented Curvilinear Operator). The proposed operator

includes an inhibition mechanism that determines the suppression of the responses due to spurious texture. We performed experiments that demonstrated the effectiveness of the proposed method on various benchmark data sets for different real-world applications, such as rose stem detection for gardening robotics, retinal blood vessel segmentation, road and river segmentation in aerial images, and crack detection in pavement and road images. The results that we obtained are better, with high statistical significance, than many other unsupervised filter-based approaches.

REFERENCES

- [1] L. Zhang, Y. Zhang, M. Wang, and Y. Li, "Adaptive river segmentation in SAR images," *J. Electron.*, vol. 26, no. 4, pp. 438–442, 2009.
- [2] P. R. Muduli and U. C. Pati, "A novel technique for wall crack detection using image fusion," in *Proc. ICCCI*, 2013, pp. 1–6.
- [3] M. Wdowiak, T. Markiewicz, S. Osowski, J. Patera, and W. Kozlowski, "Novel segmentation algorithm for identification of cell membrane staining in HER2 images," *Pattern Recognit. Lett.*, vol. 84, pp. 225–231, Dec. 2016.
- [4] M. Meijs *et al.*, "Robust segmentation of the full cerebral vasculature in 4D CT of suspected stroke patients," *Sci. Rep.*, vol. 7, no. 1, 2017, Art. no. 15622.
- [5] P. Bibiloni, M. González-Hidalgo, and S. Massanet, "A survey on curvilinear object segmentation in multiple applications," *Pattern Recognit.*, vol. 60, pp. 949–970, Dec. 2016.
- [6] C. Lacoste, X. Descombes, and J. Zerubia, "Point processes for unsupervised line network extraction in remote sensing," *IEEE Trans. Pattern Anal. Mach. Intell.*, vol. 27, no. 10, pp. 1568–1579, Oct. 2005.
- [7] Y. Verdié and F. Lafarge, "Efficient Monte Carlo sampler for detecting parametric objects in large scenes," in *Computer Vision—ECCV*. Berlin, Germany: Springer, 2012, pp. 539–552.
- [8] F. Lafarge, G. G. Farb, and X. Descombes, "Geometric feature extraction by a multimarked point process," *IEEE Trans. Pattern Anal. Mach. Intell.*, vol. 32, no. 9, pp. 1597–1609, Sep. 2010.
- [9] D. Chai, W. Förstner, and F. Lafarge, "Recovering line-networks in images by junction-point processes," in *Proc. IEEE CVPR*, Jun. 2013, pp. 1894–1901.
- [10] E. Türetken, F. Benmansour, B. Andres, P. Głowacki, H. Pfister, and P. Fua, "Reconstructing curvilinear networks using path classifiers and integer programming," *IEEE Trans. Pattern Anal. Mach. Intell.*, vol. 38, no. 12, pp. 2515–2530, Dec. 2016.
- [11] L. Chen, X. Huang, and J. Tian, "Retinal image registration using topological vascular tree segmentation and bifurcation structures," *Biomed. Signal Process. Control*, vol. 16, pp. 22–31, Feb. 2015.
- [12] M. Niemeijer, J. Staal, B. van Ginneken, M. Loog, and M. D. Abramoff, "Comparative study of retinal vessel segmentation methods on a new publicly available database," *Proc. SPIE*, vol. 5370, May 2004, pp. 648–656.
- [13] J. V. B. Soares, J. J. G. Leandro, R. M. Cesar, H. F. Jelinek, and M. J. Cree, "Retinal vessel segmentation using the 2-D Gabor wavelet and supervised classification," *IEEE Trans. Med. Imag.*, vol. 25, no. 9, pp. 1214–1222, Sep. 2006.
- [14] J. Staal, M. D. Abramoff, M. Niemeijer, M. Viergever, and B. van Ginneken, "Ridge-based vessel segmentation in color images of the retina," *IEEE Trans. Med. Imag.*, vol. 23, no. 4, pp. 501–509, Apr. 2004.
- [15] E. Ricci and R. Perfetti, "Retinal blood vessel segmentation using line operators and support vector classification," *IEEE Trans. Med. Imag.*, vol. 26, no. 10, pp. 1357–1365, Oct. 2007.
- [16] D. Marin, A. Aquino, M. E. Gegundez-Arias, and J. M. Bravo, "A new supervised method for blood vessel segmentation in retinal images by using gray-level and moment invariants-based features," *IEEE Trans. Med. Imag.*, vol. 30, no. 1, pp. 146–158, Jan. 2011.
- [17] O. Ronneberger, P. Fischer, and T. Brox, "U-Net: Convolutional networks for biomedical image segmentation," in *Proc. MICCAI*, 2015, pp. 234–241.
- [18] V. Badrinarayanan, A. Kendall, and R. Cipolla, "SegNet: A deep convolutional encoder-decoder architecture for image segmentation," *IEEE Trans. Pattern Anal. Mach. Intell.*, vol. 39, no. 12, pp. 2481–2495, Dec. 2017. doi: 10.1109/TPAMI.2016.2644615.

- [19] S. Xie and Z. Tu, "Holistically-nested edge detection," *Int. J. Comput. Vis.*, vol. 125, nos. 1–3, pp. 3–18, Dec. 2017.
- [20] W. Shen, X. Wang, Y. Wang, X. Bai, and Z. Zhang, "DeepContour: A deep convolutional feature learned by positive-sharing loss for contour detection," in *Proc. CVPR*, 2015, pp. 3982–3991.
- [21] Y. Wang, X. Zhao, and K. Huang, "Deep crisp boundaries," in *Proc. CVPR*, 2017, pp. 3892–3900.
- [22] A. F. Frangi, W. J. Niessen, K. L. Vincken, and M. A. Viergever, "Multiscale vessel enhancement filtering," in *Medical Image Computing and Computer-Assisted Intervention—MICCAI*, W. M. Wells, A. Colchester, and S. Delp, Eds. Berlin, Germany: Springer, 1998, pp. 130–137.
- [23] Y. Sato *et al.*, "Three-dimensional multi-scale line filter for segmentation and visualization of curvilinear structures in medical images," *Med. Image Anal.*, vol. 2, no. 2, pp. 143–168, 1998.
- [24] K. Krissian, G. Malandain, N. Ayache, R. Vaillant, and Y. Trouset, "Model-based detection of tubular structures in 3D images," *Comput. Vis. Image Understand.*, vol. 80, no. 2, pp. 130–171, Nov. 2000.
- [25] A. Hoover, V. Kouznetsova, and M. Goldbaum, "Locating blood vessels in retinal images by piecewise threshold probing of a matched filter response," *IEEE Trans. Med. Imag.*, vol. 19, no. 3, pp. 203–210, Mar. 2000.
- [26] M. Al-Rawi, M. Qutaishat, and M. Arrar, "An improved matched filter for blood vessel detection of digital retinal images," *Comput. Biol. Med.*, vol. 37, no. 2, pp. 262–267, 2007.
- [27] F. Zana and J.-C. Klein, "Segmentation of vessel-like patterns using mathematical morphology and curvature evaluation," *IEEE Trans. Med. Imag.*, vol. 10, no. 7, pp. 1010–1019, Jul. 2001.
- [28] A. M. Mendonca and A. Campilho, "Segmentation of retinal blood vessels by combining the detection of centerlines and morphological reconstruction," *IEEE Trans. Med. Imag.*, vol. 25, no. 9, pp. 1200–1213, Sep. 2006.
- [29] M. E. Martinez-Pérez, A. D. Hughes, S. A. Thom, A. A. Bharath, and K. H. Parker, "Segmentation of blood vessels from red-free and fluorescein retinal images," *Med. Image Anal.*, vol. 11, no. 1, pp. 47–61, 2007.
- [30] B. S. Y. Lam, Y. Gao, and A. W.-C. Liew, "General retinal vessel segmentation using regularization-based multiconcavity modeling," *IEEE Trans. Med. Imag.*, vol. 29, no. 7, pp. 1369–1381, Jul. 2010.
- [31] Y. Zhao, L. Rada, K. Chen, S. P. Harding, and Y. Zheng, "Automated vessel segmentation using infinite perimeter active contour model with hybrid region information with application to retinal images," *IEEE Trans. Med. Imag.*, vol. 34, no. 9, pp. 1797–1807, Sep. 2015.
- [32] G. Azzopardi, N. Strisciuglio, M. Vento, and N. Petkov, "Trainable COSFIRE filters for vessel delineation with application to retinal images," *Med. Image Anal.*, vol. 19, no. 1, pp. 46–57, Jan. 2015.
- [33] N. Strisciuglio, G. Azzopardi, M. Vento, and N. Petkov, "Unsupervised delineation of the vessel tree in retinal fundus images," in *Proc. VIPIMAGE*, 2015, pp. 149–155.
- [34] N. Strisciuglio, G. Azzopardi, M. Vento, and N. Petkov, "Supervised vessel delineation in retinal fundus images with the automatic selection of B-COSFIRE filters," *Mach. Vis. Appl.*, pp. 1137–1149, 2016.
- [35] O. Merveille, B. Naegel, H. Talbot, L. Najman, and N. Passat, "2D filtering of curvilinear structures by ranking the orientation responses of path operators (RORPO)," *Image Process. On Line*, vol. 7, pp. 246–261, 2017.
- [36] O. Merveille, H. Talbot, L. Najman, and N. Passat, "Curvilinear structure analysis by ranking the orientation responses of path operators," *IEEE Trans. Pattern Anal. Mach. Intell.*, vol. 40, no. 2, pp. 304–317, Feb. 2018.
- [37] J. Zhang, B. Dashtbozorg, E. Bekkers, J. P. W. Pluim, R. Duits, and B. M. ter Haar Romeny, "Robust retinal vessel segmentation via locally adaptive derivative frames in orientation scores," *IEEE Trans. Med. Imag.*, vol. 35, no. 12, pp. 2631–2644, Dec. 2016.
- [38] T. C. B. Freeman, S. Durand, D. C. Kiper, and M. Carandini, "Suppression without inhibition in visual cortex," *Neuron*, vol. 35, no. 4, pp. 759–771, Aug. 2002.
- [39] Y.-T. Li, W.-P. Ma, L.-Y. Li, L. A. Ibrahim, S.-Z. Wang, and H. W. Tao, "Broadening of inhibitory tuning underlies contrast-dependent sharpening of orientation selectivity in mouse visual cortex," *J. Neurosci.*, vol. 32, no. 46, pp. 16466–16477, 2012.
- [40] J. Kremkow *et al.*, "Push-pull receptive field organization and synaptic depression: Mechanisms for reliably encoding naturalistic stimuli in V1," *Frontiers Neural Circuits*, vol. 10, p. 37, May 2016.
- [41] S. Brincat and C. E. Connor, "Underlying principles of visual shape selectivity in posterior inferotemporal cortex," *Nature Neurosci.*, vol. 7, no. 8, pp. 880–886, Jul. 2004.
- [42] J. Guo, C. Shi, G. Azzopardi, and N. Petkov, "Inhibition-augmented trainable COSFIRE filters for keypoint detection and object recognition," *Mach. Vis. Appl.*, vol. 27, no. 8, pp. 1197–1211, Nov. 2016.
- [43] J. Guo, C. Shi, G. Azzopardi, and N. Petkov, "Inhibition-augmented COSFIRE model of shape-selective neurons," *IBM J. Res. Develop.*, vol. 61, nos. 2–3, pp. 10–1–10–9, Mar./May 2017.
- [44] N. Petkov and W. T. Visser, "Modifications of center-surround, spot detection and dot-pattern selective operators," *Inst. Math. Comput. Sci.*, Univ. Groningen, Groningen, The Netherlands, Tech. Rep. CS 2005-9-01, 2005.
- [45] D. H. Hubel and T. N. Wiesel, "Receptive fields, binocular interaction and functional architecture in the cat's visual cortex," *J. Physiol.*, vol. 160, no. 1, pp. 106–154, 1962.
- [46] R. W. Rodieck, "Quantitative analysis of cat retinal ganglion cell response to visual stimuli," *Vis. Res.*, vol. 5, no. 12, pp. 583–601, 1965.
- [47] G. E. Irvin, V. Casagrande, and T. T. Norton, "Center/surround relationships of magnocellular, parvocellular, and koniocellular relay cells in primate lateral geniculate nucleus," *Vis. Neurosci.*, vol. 10, no. 2, pp. 363–373, 1993.
- [48] B. H. Liu, Y. T. Li, W. P. Ma, C. J. Pan, L. I. Zhang, and H. W. Tao, "Broad inhibition sharpens orientation selectivity by expanding input dynamic range in mouse simple cells," *Neuron*, vol. 71, no. 3, pp. 542–554, 2011.
- [49] J. A. Solomon and D. G. Pelli, "The visual filter mediating letter identification," *Nature*, vol. 369, pp. 395–397, Jun. 1994.
- [50] C. G. Owen *et al.*, "Measuring retinal vessel tortuosity in 10-year-old children: Validation of the computer-assisted image analysis of the retina (CAIAR) program," *Invest. Ophthalmol. Vis. Sci.*, vol. 50, no. 5, pp. 2004–2010, 2009.
- [51] J. Odstrcilik *et al.*, "Retinal vessel segmentation by improved matched filtering: Evaluation on a new high-resolution fundus image database," *IET Image Process.*, vol. 7, no. 4, pp. 373–383, Jun. 2013.
- [52] N. Strisciuglio *et al.*, "TrimBot2020: An outdoor robot for automatic gardening," in *Proc. 50th Int. Symp. Robot.*, 2018, pp. 1–6.
- [53] Q. Zou, Q. Li, F. Zhang, Z. X. Q. Wang, and Q. Wang, "Path voting based pavement crack detection from laser range images," in *Proc. IEEE ICDSP*, Oct. 2016, pp. 432–436.
- [54] Q. Li, Q. Zou, D. Zhang, and Q. Mao, "FoSA: F* seed-growing approach for crack-line detection from pavement images," *Image Vis. Comput.*, vol. 29, no. 12, pp. 861–872, 2011.
- [55] Q. Zou, Y. Cao, Q. Li, Q. Mao, and S. Wang, "CrackTree: Automatic crack detection from pavement images," *Pattern Recognit. Lett.*, vol. 33, no. 3, pp. 227–238, 2012.
- [56] N. Strisciuglio, G. Azzopardi, and N. Petkov, "Detection of curved lines with B-COSFIRE filters: A case study on crack delineation," in *Computer Analysis of Images and Patterns*. Cham, Switzerland: Springer, 2017, pp. 108–120.
- [57] S. Boughorbel, F. Jaray, and M. El-Anbari, "Optimal classifier for imbalanced data using Matthews Correlation Coefficient metric," *PLOS ONE*, vol. 12, no. 6, 2017, Art. no. e0177678.
- [58] M. Vania, D. Mureja, and D. Lee, "Automatic spine segmentation from CT images using convolutional neural network via redundant generation of class labels," *J. Comput. Des. Eng.*, vol. 6, no. 2, pp. 224–232, 2019.
- [59] A. F. de Siqueira, W. M. Nakasuga, A. Pagamisse, C. A. T. Saenz, and A. E. Job, "An automatic method for segmentation of fission tracks in epidote crystal photomicrographs," *Comput. Geosci.*, vol. 69, pp. 55–61, Aug. 2014.
- [60] S. Bouix *et al.*, "On evaluating brain tissue classifiers without a ground truth," *NeuroImage*, vol. 36, no. 4, pp. 1207–1224, 2007.
- [61] M. E. Gegundez-Arias, A. Aquino, J. M. Bravo, and D. Marin, "A function for quality evaluation of retinal vessel segmentations," *IEEE Trans. Med. Imag.*, vol. 31, no. 2, pp. 231–239, Feb. 2012.
- [62] S. Chaudhuri, S. Chatterjee, N. Katz, M. Nelson, and M. Goldbaum, "Detection of blood vessels in retinal images using two-dimensional matched filters," *IEEE Trans. Med. Imag.*, vol. 8, no. 3, pp. 263–269, Sep. 1989.
- [63] X. Jiang and D. Mojon, "Adaptive local thresholding by verification-based multithreshold probing with application to vessel detection in retinal images," *IEEE Trans. Pattern Anal. Mach. Intell.*, vol. 25, no. 1, pp. 131–137, Jan. 2003.
- [64] J. I. Orlando and M. Blaschko, "Learning fully-connected CRFs for blood vessel segmentation in retinal images," in *Medical Image Computing and Computer-Assisted Intervention—MICCAI* (Lecture Notes in Computer Science), vol. 8673. Cham, Switzerland: Springer, 2014, pp. 634–641.

- [65] J. I. Orlando, E. Prokofyeva, and M. B. Blaschko, "A discriminatively trained fully connected conditional random field model for blood vessel segmentation in fundus images," *IEEE Trans. Biomed. Eng.*, vol. 64, no. 1, pp. 16–27, Jan. 2017.
- [66] H. Fu, Y. Xu, S. Lin, D. W. K. Wong, and J. Liu, "DeepVessel: Retinal vessel segmentation via deep learning and conditional random field," in *Medical Image Computing and Computer-Assisted Intervention—MICCAI*. Cham, Switzerland: Springer, 2016, pp. 132–139.
- [67] M. Rochery, I. H. Jermyn, and J. Zerubia, "Higher order active contours," *Int. J. Comput. Vis.*, vol. 69, no. 1, pp. 27–42, Aug. 2006.
- [68] N. Strisciuglio and N. Petkov, "Delineation of line patterns in images using *B*-COSFIRE filters," in *Proc. IWobi*, 2017, pp. 1–6.
- [69] F. Liu, G. Xu, Y. Yang, X. Niu, and Y. Pan, "Novel approach to pavement cracking automatic detection based on segment extending," in *Proc. Int. Symp. Knowl. Acquisition Modeling*, 2008, pp. 610–614.
- [70] D. Martin, C. Fowlkes, D. Tal, and J. Malik, "A database of human segmented natural images and its application to evaluating segmentation algorithms and measuring ecological statistics," in *Proc. ICCV*, vol. 2, Jul. 2001, pp. 416–423.
- [71] G. Azzopardi, L. Fernández-Robles, E. Alegre, and N. Petkov, "Increased generalization capability of trainable COSFIRE filters with application to machine vision," in *Proc. IEEE ICPR*, Dec. 2016, pp. 279–291.
- [72] N. Strisciuglio, G. Azzopardi, M. Vento, and N. Petkov, "Multiscale blood vessel delineation using *B*-COSFIRE filters," in *Computer Analysis of Images and Patterns* (Lecture Notes in Computer Science), vol. 9257. Cham, Switzerland: Springer, 2015, pp. 300–312.
- [73] G. Azzopardi and N. Azzopardi, "Trainable COSFIRE filters for key-point detection and pattern recognition," *IEEE Trans. Pattern Anal. Mach. Intell.*, vol. 35, no. 2, pp. 490–503, Feb. 2013.
- [74] B. Gecer, G. Azzopardi, and N. Petkov, "Color-blob-based COSFIRE filters for object recognition," *Image Vis. Comput.*, vol. 57, pp. 165–174, Jan. 2017.
- [75] N. Strisciuglio, M. Vento, and N. Petkov, "Bio-inspired filters for audio analysis," in *Proc. BrainComp*, 2016, pp. 101–115.
- [76] N. Strisciuglio, M. Vento, and N. Petkov, "Learning sound representations using trainable COPE feature extractors," *Pattern Recognit.*, vol. 92, pp. 25–36, Mar. 2019.
- [77] A. Saggese, N. Strisciuglio, M. Vento, and N. Petkov, "Learning skeleton representations for human action recognition," *Pattern Recognit. Lett.*, vol. 118, pp. 23–31, Feb. 2018.
- [78] M. López-Antequera, M. Leyva-Vallina, N. Strisciuglio, and N. Petkov, "Place and object recognition by CNN-based COSFIRE filters," *IEEE Access*, vol. 7, pp. 66157–66166, 2019.



Nicola Strisciuglio received the Ph.D. degree (*cum laude*) in computer science from the University of Groningen, The Netherlands, in 2016, and the Ph.D. degree in information engineering from the University of Salerno, Italy, in 2017. He is currently a Post-Doctoral Researcher with the Bernoulli Institute for Mathematics, Computer Science and Artificial Intelligence, University of Groningen. His research interests include pattern recognition, machine learning, signal processing, and computer vision. He was the General Co-Chair of the First and Second International Conference on Applications of Intelligent Systems (APPIS) in 2018 and 2019.



George Azzopardi received the B.Sc. degree (Hons.) from Goldsmiths, the M.Sc. degree from the Queen Mary University of London, and the Ph.D. degree (*cum laude*) in computer science from the University of Groningen, in 2013. He is currently an Assistant Professor of computer science with the University of Groningen, The Netherlands. He co-promoted three Ph.D. candidates so far and is also a participant in the EU H2020 project 4NSEEK. He has (co)authored more than 50 peer-reviewed publications. His research interests include image processing, pattern recognition, machine learning, medical image analysis, and information systems. He is an Associate Editor of a Q1 journal.



Nicolai Petkov received the Dr.sc.techn. degree in computer engineering (informationstechnik) from the Dresden University of Technology, Dresden, Germany. Since 1991, he has been a Professor of computer science and the Head of the Intelligent Systems Group, University of Groningen. He has authored two monographs and has authored or coauthored over 200 scientific papers. He holds four patents. His current research interests include pattern recognition, machine learning, data analytics, and brain-inspired computing, with applications in healthcare, finance, surveillance, manufacturing, robotics, and animal breeding. He is a member of the editorial board of several journals.